Supporting Information

Topotactic phase transformations by concerted dual-ion migration of B-site cation and oxygen in multivalent cobaltite La-Sr-Co-O$_x$ films

Jia Li[#a,b], Meng-Xue Guan[#a,b], Peng-Fei Nan[c], Jing Wang*[a,b], Bing-Hui Ge*[c], Kai-Ming Qiao[a,b], Hong-Rui Zhang[a,b], Wen-Hui Liang[a,b], Jia-Zheng Hao[a], Hou-Bo Zhou[a,b], Fei-Ran Shen[a,b], Fei-Xiang Liang[a,b], Cheng Zhang[a,b], Miao Liu[a,b], Sheng Meng[a,b,d], Tao Zhu*[a,d,f], Feng-Xia Hu*[a,b,d], Tom Wu[e], Jian-Dong Guo[a,b,d], Ji-Rong Sun[a,b,d] & Bao-Gen Shen*[a,g,b,d]

[a] Beijing National Laboratory for Condensed Matter Physics, Institute of Physics, Chinese Academy of Sciences, Beijing, 100190, PR China.

[b] School of Physical Sciences, University of Chinese Academy of Sciences, Beijing, 100049, PR China.

[c] Institute of Physical Science and Information Technology, Anhui University, Hefei, Anhui, 230601, PR China.

[d] Songshan Lake Materials Laboratory, Dongguan, Guangdong, 523808, PR China.

[e] School of Materials Science and Engineering, University of New South Wales (UNSW), Sydney, NSW 2052, Australia.

[f] Spallation Neutron Source Science Center, Dongguan, 523803, PR China.

[g] Institute of Rare Earths, Chinese Academy of Sciences, Jiangxi, 341000, PR China.

Email: fxhu@iphy.ac.cn; wangjing@iphy.ac.cn; shenbg@iphy.ac.cn; bhge@ahu.edu.cn; tzhu@iphy.ac.cn

Note S1: Annealing conditions.

Annealing experiments under varying vacuum, temperature, duration time and rates of heating and cooling have been performed to ascertain appropriate conditions for producing topotactic transformation. Firstly, we found that the high vacuum is one requirement for obtaining 1125-LSCO and 214-LSCO samples via topotactic transformation. However, the 1125-LSCO, especially 214-LSCO phase seldom appears upon vacuum annealing when the vacuum pressure is higher than 10^{-4}Pa. This is understandable since the transformations from 113-LSCO to 1125-LSCO and to

214-LSCO structure correlate with the reduction of Co ions.

Meanwhile, we found that the vacuum annealing temperature strongly affects the transition ratio for the both steps of perovskite-browmillerite (P-BM) and browmillerite-single layered pervoskite (BM-SL). Figure S1 shows the collected XRD patterns for La-Sr-Co-O_x films vacuum annealed (10^{-6}Pa) for 15min under different temperatures of 150, 300, 400 and 450℃, respectively. One can find that clean BM characteristic peaks of BM-(004),(006) and (008) at about 22.3°, 33.8° and 45.7° appear when the vacuum annealing temperature reaches 300℃, while clean SL characteristic peaks of SL-(004) and (006) at about 28.2° and 42.9° emerge with the annealing temperature reaching 450 ℃. It suggests that complete topotactic transformations of perovskite to BM and BM to SL were obtained at vacuum annealing temperatures of 300℃ and 450℃, respectively. With the vacuum annealing temperature at 150℃, the coexistence of oxygen deficient perovskite and 1125-LSCO phases appears in the film, indicated by the broadening and splitting of BM characteristic peaks (see green trace in Fig. S1), demonstrating the incomplete transformation from perovskite to BM phase. While under the vacuum annealing temperature of 400℃, the coexistence of characteristic peaks of both BM and SL phases (purple trace) indicates that the film undergoes an incomplete transformation from BM to SL phase.

On the other hand, our experiments showed that the pure 214-LSCO phase can be obtained only when the ramping rate of temperature is fast enough for annealing, implying that the 214-LSCO phase appears to be a metastable state. For example, with a low heating rate of 10℃/min and cooling rate of 4 ℃/min, no 214-LSCO phase was observed even when the vacuum annealing temperature was set up to 500℃. Meanwhile, it was found that the perovskite-BM transformation is relatively insensitive to the heating/cooling rate.

Finally, vacuum of 10^{-6} Pa, annealing temperature of 300℃ and 450℃, and annealed duration time of 15min were chosen to induce the tri-state topotactic transformation. Meanwhile, the heating and cooling rate were set as 200℃/min and

14°C/min, respectively, in view of the easy realization and satisfactory results.

Note S2: Variation of chemical valence state of Co ions during the topotactic phase transformation.

In the process of oxygen and cobalt ions transfer, three states of 113-LSCO, 1125-LSCO and 214-LSCO appear, respectively. In XPS O-$1s$ spectra for three films, the peak of oxygen deficiency is recognized at about 531 eV (Fig. S7b).[S1] It is seen that the intensity of oxygen vacancies gets higher during the topotactic transformations, which is an evidence for the increase of oxygen vacancies.

The EELS measurements (detecting range: ~0.2nm) were performed focusing on the area of 113-LSCO, 1125-LSCO and 214-LSCO phases to further analyze the valence state (Fig. S6). For the O K-edge shown in Fig. S6b, peak A, B and C represent the Co $3d$-O $2p$, La $5d$-O $2p$/Sr $4d$-O $2p$ and Co $4s$-O $2p$ hybridization, respectively.[S2] The very low intensity of the peak A demonstrates that the cobalt oxidation in 1125-$La_{0.7}Sr_{0.3}CoO_{2.5}$ and 214-$La_{1.4}Sr_{0.6}CoO_4$ films is relatively weak. The intensity ratios of Co L_3/L_2 were calculated after subtracting the background of each spectrum and plotted in the fitting curve of L_3/L_2 $vs.$ Co valence (Fig. S6a).[S3] In this way, the Co valence states are estimated from the fitting curve as +2.78, +2.38 and +2.46 for 113-$La_{0.7}Sr_{0.3}CoO_3$, 1125-$La_{0.7}Sr_{0.3}CoO_{2.5}$ and 214-$La_{1.4}Sr_{0.6}CoO_4$ phases, respectively. This method has been well accepted to quantitatively estimate the valence of Co-ions in cobalt oxide.[S3,S4] Note that the calculated valence state of cobalt in $La_{0.7}Sr_{0.3}CoO_3$ is lower than the theoretical value (+3.30), which is ascribed to the deoxidization during the preparation of cross sectional specimens by using focused ion beam and electron beam irradiation.[S5] More interestingly, the valence state of Co in 214-LSCO is higher than that in 1125-LSCO, disagreeing with the results of XAS where the obtained average valence state of cobalt in La-Sr-Co-O_x films exhibits a monotonous reduction during the continuous topotactic phase transformations from 113-LSCO to 1125-LSCO and to 214-LSCO. However, such increased valence state in 214-LSCO phase detected by EELS is consistent with the theoretical values calculated from the chemical formula (+2.30 for 1125-

3

La$_{0.7}$Sr$_{0.3}$CoO$_{2.5}$ and +2.60 for 214- La$_{1.4}$Sr$_{0.6}$CoO$_4$).

It is worth noting that the detecting area of XAS (~50nm) is much larger than that of EELS (~0.2nm). Meanwhile, the EELS measurements were definitely focusing on 214-LSCO structure (determined from STEM observations). Thus, the opposite evolution trend of Co valence state for XAS and EELS measurements implies that lower valence or elementary Co atoms may exist in the 214-film. Considering that the B-site cobalt ions migrated out from the frame structure of BM 1125-LSCO cannot release to ambient atmosphere, one can conclude that the reduction of average Co valence for 214-LSCO film indicated by XAS measurements should originate from the contribution of the migrated Co locating in the 214-LSCO film, which pulls down the average cobalt valence of the whole film. Further XPS measurements detected two strong Co-metal peaks at 778.6 eV and 793.6 eV (Fig.4c), which correspond metallic elemental Co[S6,S7]. This result strongly suggests that the Co atoms migrated out from the structure framework of 1125-LSCO assemble together and form Co-rich areas, that is composed mainly by elementary Co, in the 214-LSCO matrix (see Fig.5).

Moreover, EELS measurements were also performed on the cluster regions (see Fig.5), which shows that the intensity ratio of Co/La in the cluster region (~2.0, see the right part of Fig. 4d) is much higher than that in 214-LSCO crystalline region (~0.14). Meanwhile, the EELS O K-edge intensity in such cluster region is almost a quarter of that in 214-crystalline region (the left part of Fig. 4d). These results also strongly evidence the Co-rich nature of the clusters.

Note S3: First-principles calculations.

To quantitatively characterize the ease of atom flowing out from the BM structural frame, we further calculated the cohesive energy, E_c, for different site atoms in La$_{0.625}$Sr$_{0.375}$CoO$_{2.5}$ by using first-principles calculations, which is defined as:

$$E_c = (E_{defect} + NE_i - E_{tot})/N \ , \tag{1}$$

where E_{tot} is the total energy of primitive BM structure, E_{defect} is the energy of BM structure with a A-site, B-site or an oxygen vacancy, E_i is the energy per Co/La(Sr) atom in the elemental solid or O atom in the oxygen molecule, N is the number of

vacancy. As shown in Fig. S8b, the cobalt vacancy in the CoO_4 tetrahedral sub-layer has a lower E_c (0.58 eV per $La_{0.625}Sr_{0.375}CoO_{2.5}$ unit cell) in comparison with oxygen vacancy (0.61 eV per $La_{0.625}Sr_{0.375}CoO_{2.5}$ unit cell) in the CoO_6 octahedral sub-layer. These results demonstrate that the CoO_4 in 1125-LSCO is more unstable and more likely to collapse. As a result, the Co-O bond in the tetrahedral sub-layer of BM 1125-LSCO tends to break down firstly with an extra energy provided and release the cobalt atoms in its framework, leading to a distinct B-site cobalt ions flowing/migration.

The density of state was also calculated for the optimized 5/8 La-doped BM structure to check the electronic structure. The result exhibits an obvious asymmetry for spin up and spin down (Fig. S8c), which reflects the magnetism and half metal properties in 1125-LSCO. By using the calculated total energy of BM $La_{0.625}Sr_{0.375}CoO_{2.5}$ and $SrCoO_{2.5}$, single-layered $La_{1.25}Sr_{0.75}CoO_4$ and Sr_2CoO_4, We calculated the reaction enthalpy changes of BM $La_{0.625}Sr_{0.375}CoO_{2.5}$ and $SrCoO_{2.5}$ to single-layered structure, respectively (Fig. S8a). The obtained enthalpy change from $La_{0.625}Sr_{0.375}CoO_{2.5}$ to $La_{1.25}Sr_{0.75}CoO_4$ is 1.49 eV, while the one from $SrCoO_{2.5}$ to Sr_2CoO_4 is 1.86 eV. This result indicates that the doping of La at A-site reduces the thermodynamic barrier of the system from a brownmillerite structure to a single-layered perovskite structure.

Note S4: The influence of La^{3+}-doping on the valence state of Co ions and stability of CoO_4 tetrahedral layer

Previous EELS and XPS measurements on $SrCoO_{2.5}$ film [S8,S9] demonstrated that the Co ions in CoO_4 sub-layer of $SrCoO_{2.5}$ film tend to show a lower valence state (Co^{2+}, for example) than those in CoO_6 sub-layer. Takayoshi Kishida et al.[S8] revealed distinct difference in the Co L-edge (and O K-edge) for Co-O planes in adjacent CoO_4 tetrahedral and CoO_6 octahedral layer (see Fig. S9a) by performing local EELS experiments on BM $SrCoO_{2.5}$. It was found that the CoO_4 layer exhibits a larger L_3/L_2 ratio than the adjacent CoO_6 layer, which indicates a lower oxidation state for the Co ions in CoO_4 tetrahedral layers[S3]. More recently, A. M. Narayanan et al. observed a

signal of Co^{2+} other than the normal Co^{3+} in XPS experiments in BM $SrCoO_{2.5}$ [Ref. S9], as shown in Fig. S9b, demonstrating the existence of Co^{2+} in the $SrCoO_{2.5}$ with the same 1125-BM structure.

As for our 1125-LSCO sample, the substitution of La^{3+} for Sr^{2+} and the resulted possible charge transfer caused by covalent sharing may make the Co valence in CoO_4 (Co^{2+}) tend to be lower, noting that the 1125-LSCO retains the same BM structure. Our quantitative analysis of the Co valence by comparing the peak intensity ratios of L_3/L_2 in the Co L-edge EELS data with reference spectra [S10] have provided an average Co valence state of +2.38 for present 1125-LSCO (see Fig. S6 and Note S2), which is roughly consistent with the theoretical value calculated from the chemical formula of $La_{0.7}Sr_{0.3}CoO_{2.5}$ (+2.30), despite of the small divergence that probably originates from the possible small off-stoichiometry in the 1125-LSCO sample. Meanwhile, the deduced average Co valence of 1125-LSCO from EELS data is lower than the theoretical one of $SrCoO_{2.5}$ (+3, calculated from the chemical formula) with the same 1125-BM structure. This result implies that the La^{3+}-doping makes the average Co valence in CoO_4 tend to reduce in comparison with the case of $SrCoO_{2.5}$, which causes the instability of Co-O bond in CoO_4 for 1125-LSCO.

Actually, experiments and theoretical calculations have both demonstrated that the 1125-LSCO with substitution of Sr^{2+} by La^{3+} shows high thermodynamic instability compared to $SrCoO_{2.5}$. The calculated reaction enthalpy change (see Note S3) of BM-to-SL phase transformation for 1125-LSCO (1.49eV) is lower than that of $SrCoO_{2.5}$ without La^{3+} doping (1.86eV), which indicates that the La^{3+} doping at A-site reduces the thermodynamic barrier for the transformation from 1125-LSCO to 214-LSCO phase. Moreover, the thermodynamic instability of CoO_4 tetrahedrons compared to CoO_6 octahedrons in 1125-LSCO was further demonstrated by theoretical calculations on cohesive energy. It was found that the CoO_4 tetrahedral sub-layer has a lower cohesive energy(0.58 eV/u.c.) than that (0.61 eV/u.c.) of the CoO_6 octahedral sub-layer (see Note S3), indicating that the break-up of Co-O bond prefers to occur in the CoO_4 sub-layers rather than in the CoO_6 octahedrons under vacuum annealing. In other words, the CoO_4 tetrahedral sub-layer in 1125-LSCO is more instable than CoO_6 octahedral sub-layer.
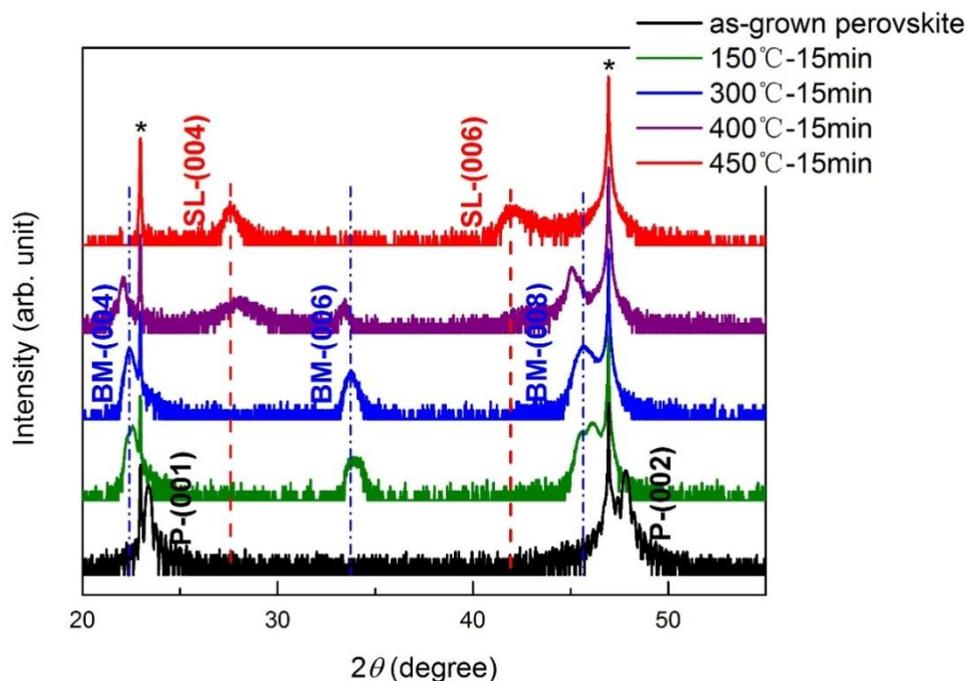
Figure S1. Collected XRD patterns for La-Sr-Co-O$_x$ films vacuum annealed (10^{-6}Pa) for 15min at 150, 300, 400 and 450℃, respectively. For comparison, the result for as-gown 113-perovskite film is also plotted. The diffraction peaks marked by asterisks come from substrate LSAT (001) and LSAT (002) peaks, respectively. P-(001) and P-(002) indicate perovskite characteristic peak, BM-(004), BM-(006) and BM-(008) are characteristic peaks of 1125-LSCO, while SL-(004) and SL-(006) are the ones of 214-LSCO phase.
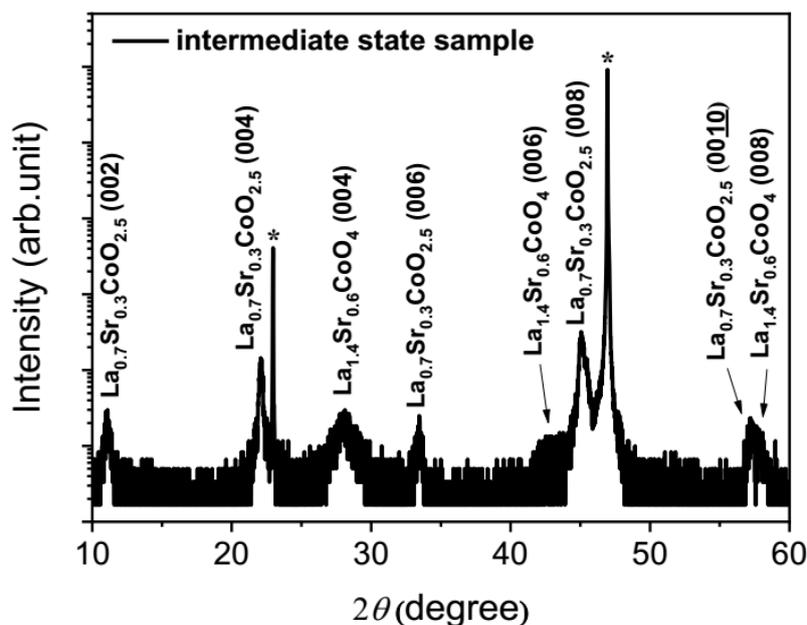
Figure S2. XRD results of intermediate state sample. The crystal plane corresponding to the diffraction peak has been marked in the figure. The diffraction peaks marked by an asterisk are

7

LSAT (001) peak and LSAT (002) peak, respectively. The results show the coexistence of 1125-LSCO and 214-LSCO in the film, indicating that no intermediate structure exists in the topotactic phase transformation from 1125-LSCO to 214-LSCO.
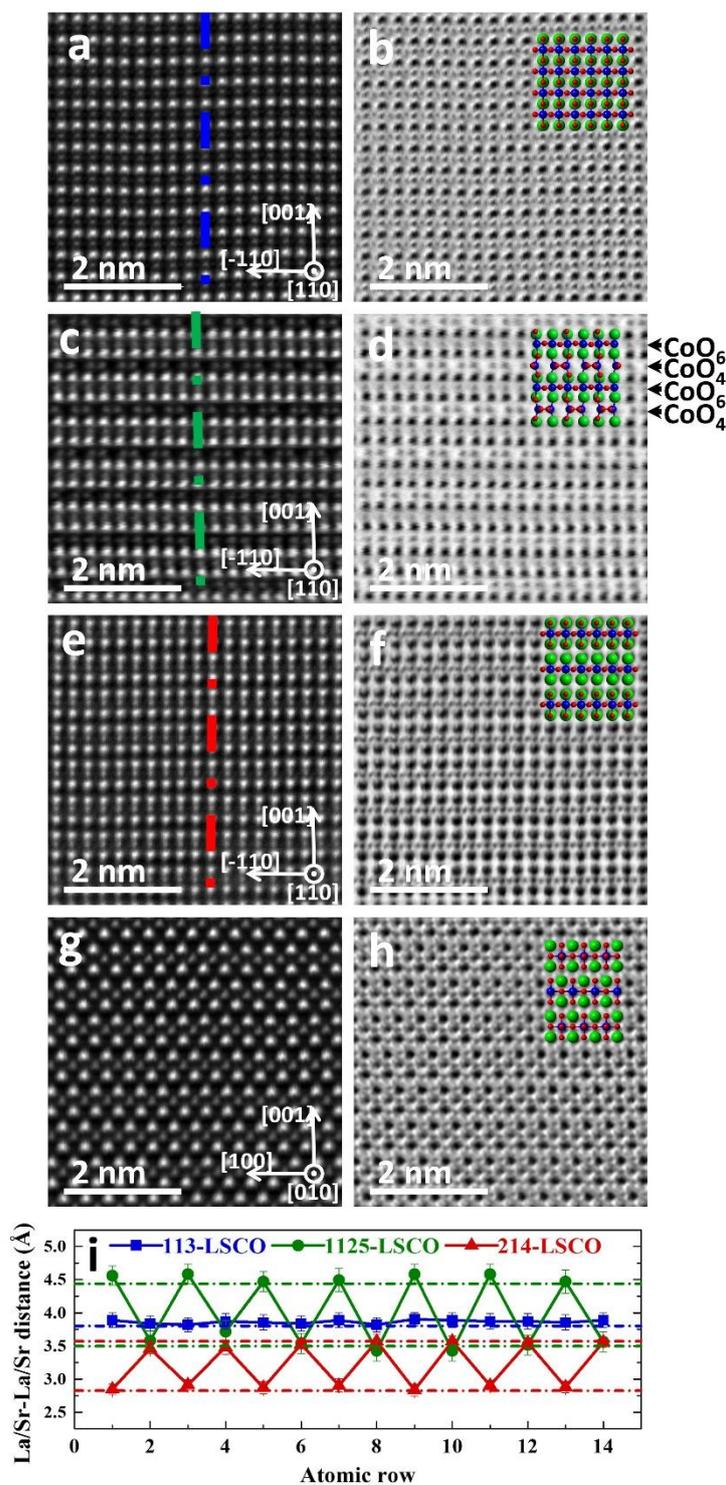
Figure S3. HAADF images of (a)113-LSCO film, (c)1125-LSCO film and (e,g) 214-LSCO film. ABF images of (b)113-LSCO film, (d)1125-LSCO film and (f,h) 214-LSCO film. The zone axis in images (a)-(f) are along the [110] LSAT direction, and (g)-(h) images along [010]. Atoms at A-, B-

and O- sites are indicated by green, violet and red spheres, respectively. (i) Comparison of statistical analysis of HAADF-STEM results (symbols) with XRD results (dashed lines) for out-of-plane La/Sr-La/Sr atomic layers distances of 113-LSCO (blue), 1125-LSCO (green) and 214-LSCO films (red). The data was extracted from (a,c,e) images along dashed lines in respective images.
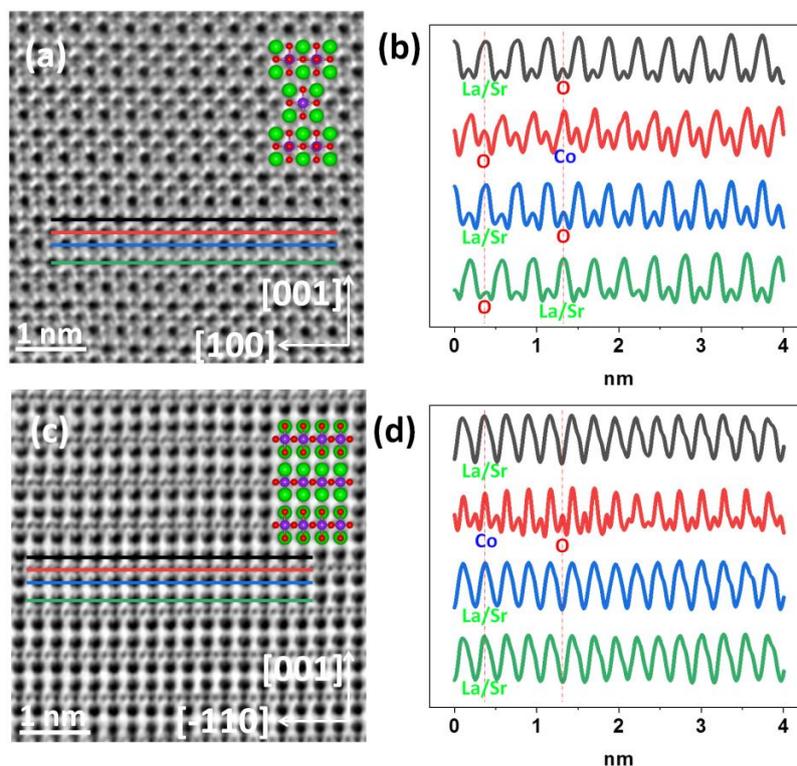
Figure S4. ABF-STEM images of the $La_{1.4}Sr_{0.6}CoO_4$ film seen along (a) [010] and (c) [110] LSAT direction. Line profiles of inversed ABF contrast of (b) Fig. S4a and (d) S4b. The positions corresponding to the different color curves have been marked with lines of the same color in the ABF images. Based on the results of ABF images we can determine that there are six oxygen ions around each cobalt ion and it is confirmed that sample S is the SL structure.
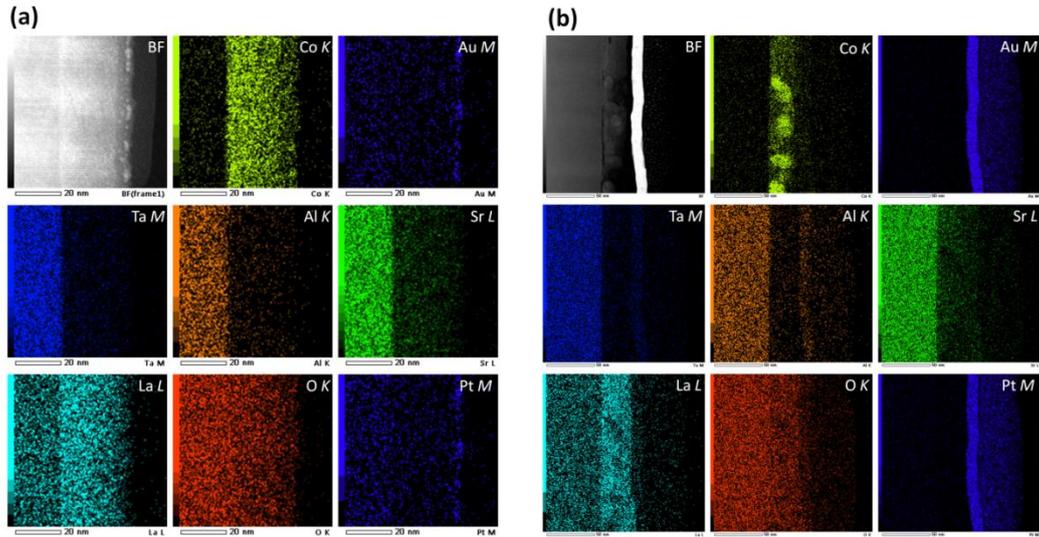
Figure S5. Cross-sectional EDS results for (a)113-LSCO and (b) 214-LSCO films. From the EDS results, excellent uniformity was determined for the as-grown samples. Some cobalt-rich regions exist in the 214-LSCO film, which is leaded by the flow of half of cobalt atoms in the film.
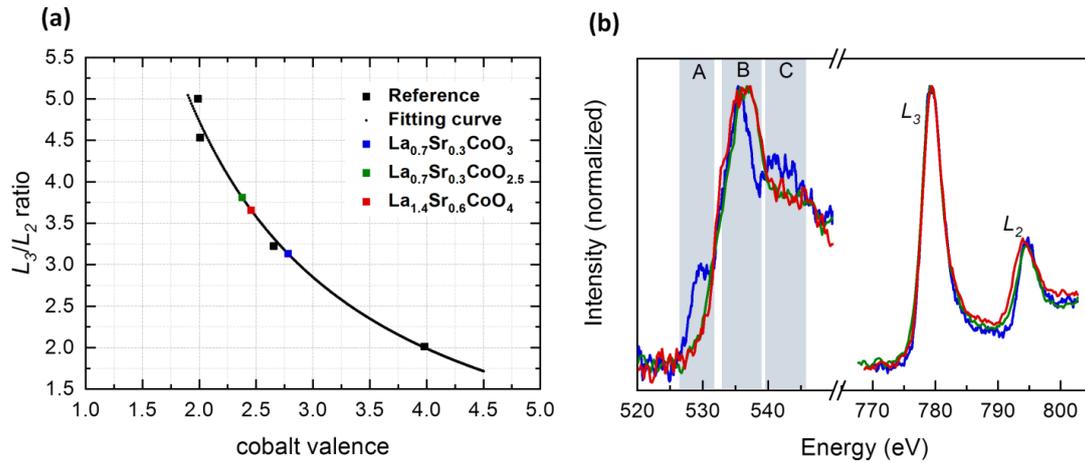
Figure S6. EELS measurements and analysis of $La_{0.7}Sr_{0.3}CoO_3$, $La_{0.7}Sr_{0.3}CoO_{2.5}$ and $La_{1.4}Sr_{0.6}CoO_4$ films, grown on LSAT(001) substrate. (a) Cobalt valence states analysis by calculating the intensity ratio of L_3/L_2 in Co L-edge EELS results. The black squares are extracted from the reference.[S3] The black line is a fitting of four black squares. After subtracting the background, the L_3/L_2 ratio is calculated and plotted together with the fitting curve. (b) O K-edge and Co L-edge EELS results for three phases. Peak A, B and C represent the Co $3d$-O $2p$, La $5d$-O $2p$/Sr $4d$-O $2p$ and Co $4s$-O $2p$ hybridization, respectively.[S2] In Co L-edge EELS results, the peak position of Co L_3 edge in each spectrum has been shifted to a same energy in order to demonstrate clearly the intensity variations of Co L_2 edge.
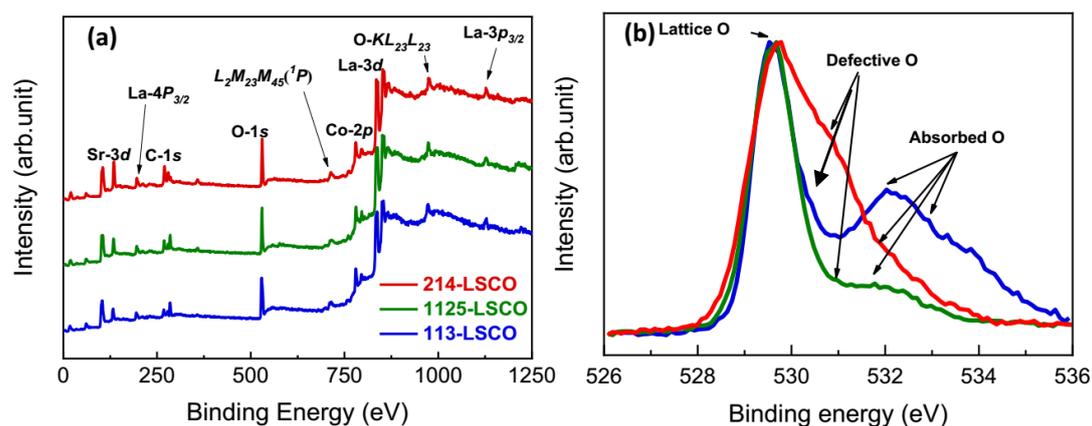
Figure S7. XPS measurements of 113-LSCO, 1125-LSCO and 214-LSCO films, grown on LSAT(001) substrate. (a) The XPS survey spectrums for three films. The peaks represent the electron binding energies of specific atomic orbitals for selected elements. $L_2M_{23}M_{45}$ and $KL_{23}L_{23}$ refer to states in Auger electron spectroscopy. No characteristic peaks other than the elements contained in the sample appear in the spectrum. (b) XPS O-1s spectra for three films. The lattice oxygen, defective oxygen and the absorbed oxygen have been marked in the figure according to the references. The peaks at 529.6 eV represent the lattice oxygen.[S1] The peak of oxygen deficiency locates at about 531 eV.[S1] While the peaks locating at the range of 532-533.5 eV represent the absorbed oxygen, which is attributed to the absorption of water, oxygen and organic oxygen on the film surfaces.[S1,S11] During the structure evolution process, the intensity of the peak representing oxygen vacancies gets higher, which is an evidence for the increase of oxygen vacancies.
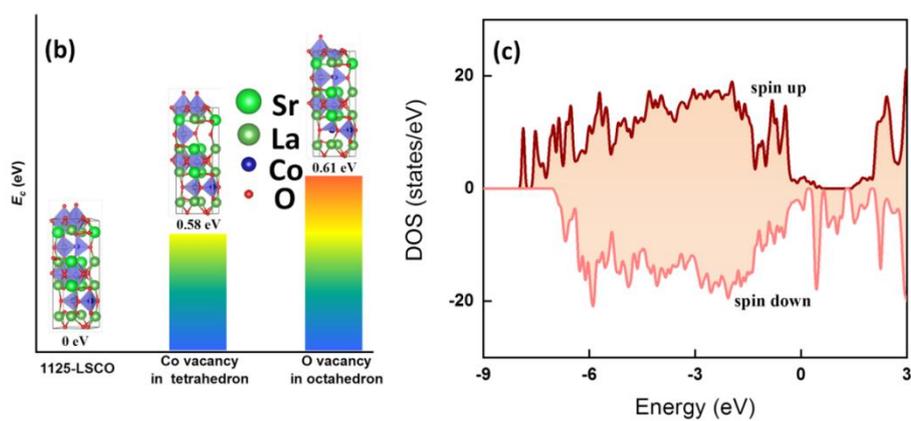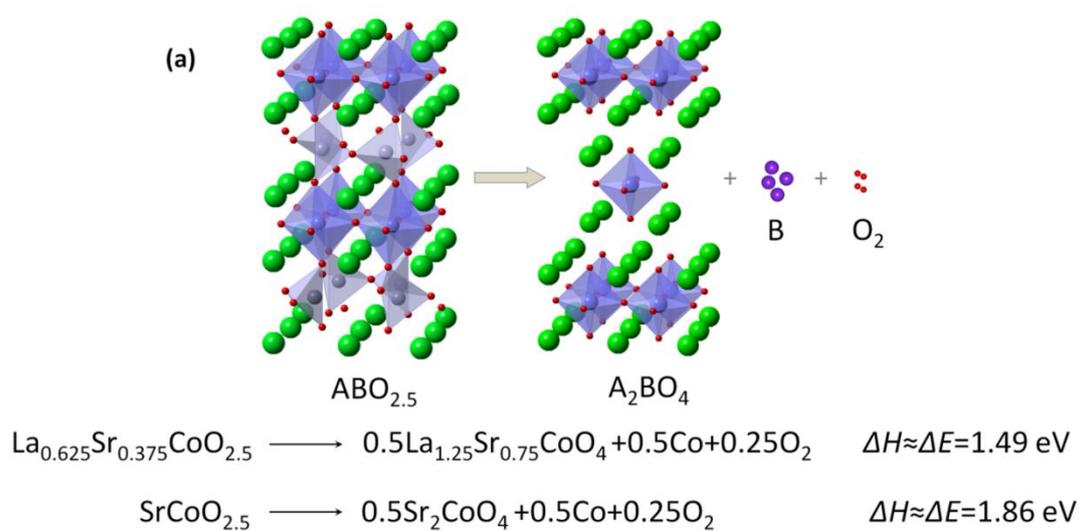
Figure S8. First-principles calculations results. (a) The reaction enthalpy of the decomposition of La$_{0.625}$Sr$_{0.375}$CoO$_{2.5}$ and SrCoO$_{2.5}$ at 0 K. (b) The 1125-LSCO cohesive energy, E_c of two possible situations: cobalt vacancy in tetrahedron and oxygen vacancy in octahedron. (c) Total densities of states for 1125-LSCO.
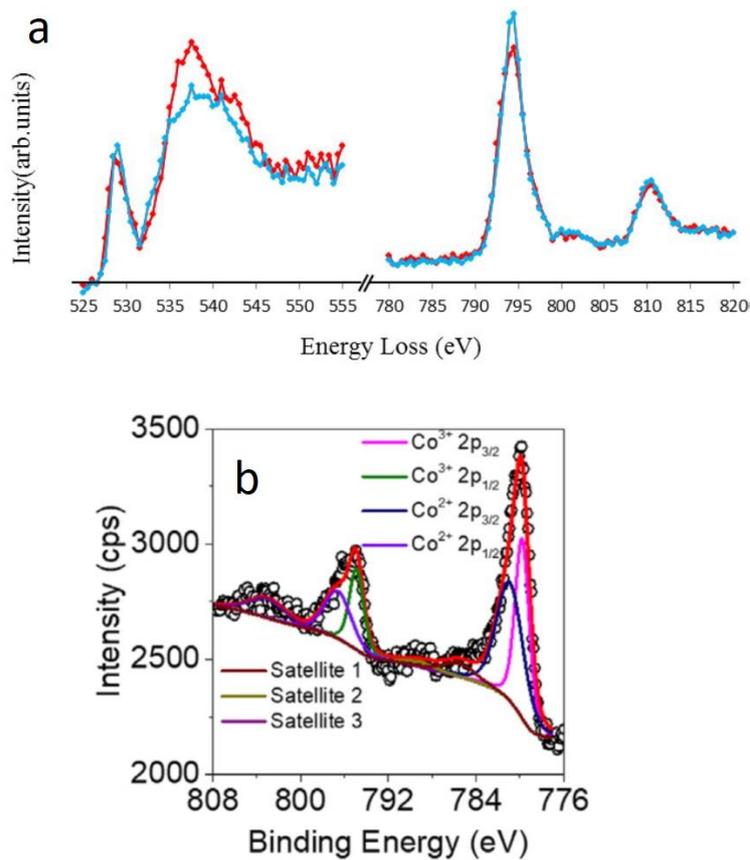
Figure S9. (a) Electron energy-loss spectra obtained from SrCoO$_{2.5}$ viewed along the c axis, showing the O K edge and the Co L$_{2,3}$ edge from alternating Co-O planes. The blue lines are from planes containing the oxygen vacancies and red lines are obtained from the fully oxygenated planes [Ref. S6, Fig.8c wherein]. (b) X-Ray photoelectron core level spectra of 1125-BM SrCoO$_{2.5}$ at Co 2p region. [Ref. S7, Fig.3 wherein].

13
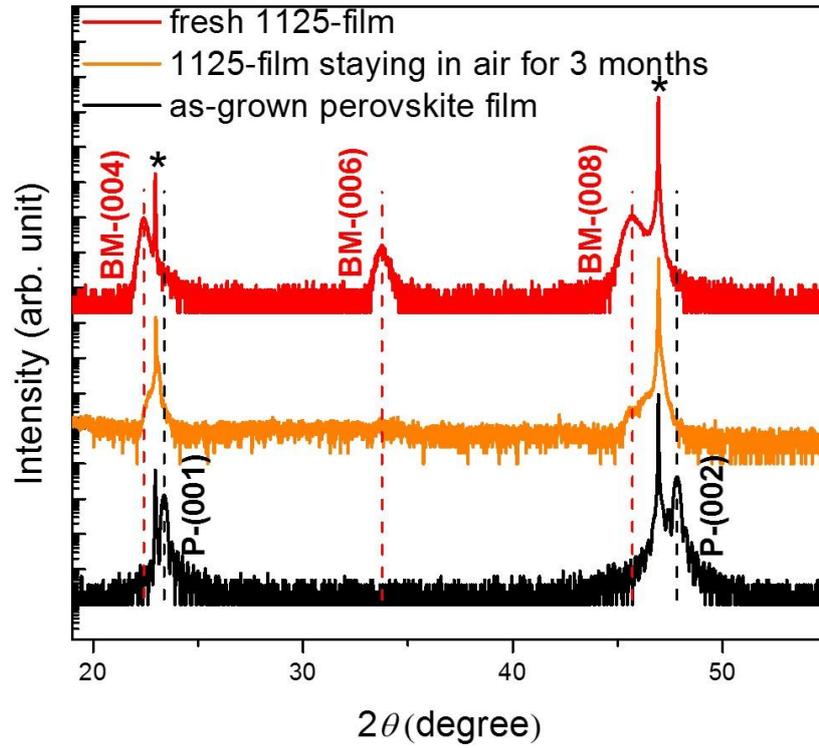
Figure S10. XRD *θ-2θ* scans of fresh 1125-film and 1125-film exposure to air for 3 months. For comparison, the data of as-grown perovskite-film is also plotted in the figure. The diffraction peaks marked by asterisks come from substrate LSAT (001) and LSAT (002) peaks, respectively. P-(001) and P-(002) indicate perovskite characteristic peaks, BM-(004), -(006) and –(008) denote BM characteristic peaks.
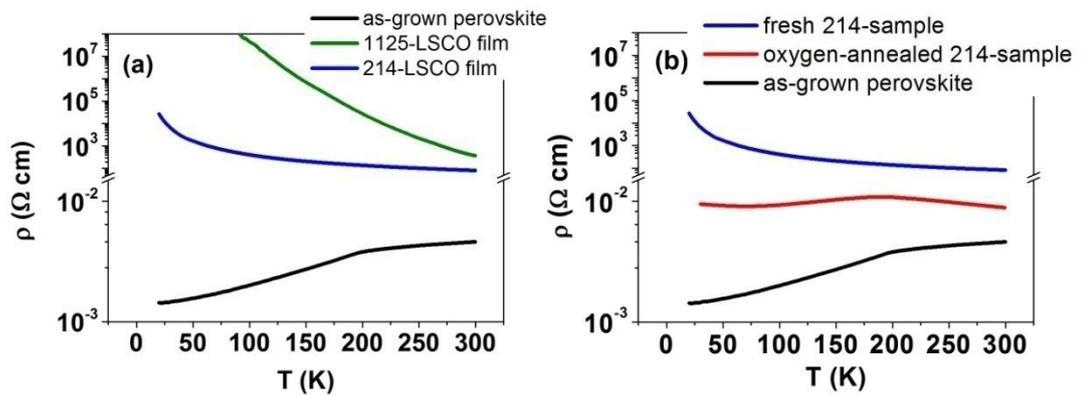
Figure S11. (a) Temperature-dependent electrical resistivity (ρ) of as-grown perovskite, 1125-LSCO and 214-LSCO films in the process undergoing vacuum annealing. (b) Temperature-dependent ρ of fresh and oxygen-annealed 214-film in comparison to the as-grown perovskite film. For comparison, the vertical axis of (a) and (b) takes the same logarithmic

coordinate.

Table S1. EDS standardless quantitative analysis for $La_{1.4}Sr_{0.6}CoO_4$ film in crystalline structure region and Co-rich region. The chemical composition of crystalline structure region is very similar to the $La_{1.4}Sr_{0.6}CoO_4$ formula. In Co-rich region, the cobalt atomic percentage is as high as 68.4%. The presence of small amounts of La, Sr and O may be caused by a small amount of crystalline $La_{1.4}Sr_{0.6}CoO_4$ wrapping the Co-rich clusters.

element	(keV)	214-crystalline region			cobalt-rich region		
		Mass%	Counts	Atom%	Mass%	Counts	Atom%
O K	0.525	15.2	780.47	53.2	4.2	97.55	16.5
Co K	6.924	15.5	839.31	14.7	64.3	757.75	68.4
Sr L	1.806	17.5	421.56	11.2	3.2	17.22	2.3
La L	4.65	51.8	1161.46	20.9	28.3	138.82	12.8
Total		100		100	100		100

15

References:

[S1] M. C. Biesinger, B. P. Payne, A. P. Grosvenor, L. W. M. Lau, A. R. Gerson and R. S. C. Smart, *Appl. Surf. Sci.,* 2011, **257,** 2717-2730.

[S2] R. F. Klie, J. C. Zheng, Y. Zhu, M. Varela, J. Wu and C. Leighton, *Phys. Rev. Lett.,* 2007, **99,** 047203.

[S3] Wang, Z. L. & J. S. Yin, *Philos. Mag. B* 1998, **77**, 49.

[S4] Q. Zhang, X. He, J. Shi, N. Lu, H. Li, Q. Yu, Z. Zhang, L. Q. Chen, B. Morris, Q. Xu, P. Yu, L. Gu, K, Jin, and   C. W. Nan, *Nat. Commun.,* 2017, **8,** 104.

[S5] Q.Q. Lan, X. J. Zhang, X. Shen, H. W. Yang, H. R. Zhang, X.X. Guan, W. Wang, Y. Yao, Y. G. Wang, Y. Peng, B. G. Liu, J. R. Sun and R. C.Yu, *Phys. Rev. Mater.,* 2017, **1,** 024403.

[S6] M. C. Biesinger, B. P. Payne, A. P. Grosvenor, L. W. M. Lau, A. R. Gerson and R. S. C. Smart, *Appl. Surf. Sci.,* 2011, **257,** 2717-2730.

[S7] A. S. Walton, J. Fester, M. Bajdich, M. A. Arman, J. Osiecki, J. Knudsen and A. Vojvodic, J. V. Lauritsen, *ACS Nano,* 2015, **9,** 2445-2453.

[S8] T. Kishida, S. J. Pennycook, and M. F. Chisholm, *Microsc. Microanal.* 2013, **19**, 1962.

[S9] Aswathy M. Narayanan, Arun M. Umarji, *J. Alloys Compd.* 2019, **803,** 102-110.

[S10] Wang, Z. L. & J. S. Yin, *Philos. Mag. B* 1998, **77**, 49.

[S11] D. Yang, A. Velamakanni, G. Bozoklu, S. Park, M. Stoller, R. D. Piner, S. Stankovich, I, Jung, D. A. Field, C. A. Ventrice, and R. S. Ruoff, *Carbon,* 2009, **47,** 145-152.